DETECTION OF A CHARACTERISTIC LENGTH IN 2D ORTHOTROPIC MICROPOLAR CONTINUUM

ODREĐIVANJE KARAKTERISTIČNE DULJINE RAVNINSKOG ORTOTROPNOG MIKROPOLARNOG KONTINUUMA

Damjan Jurković[*], **Gordan Jelenić**[*], **Sara Grbčić Erdelj**[*], **Dragan Ribarić**[*], **Laura Grbac**[*], **Edita Papa Dukić**[*], **Nina Čeh**[*]

Abstract

With the aim of obtaining several micropolar engineering parameters, a numerical and experimental analysis of an artificially generated orthotropic microstructure is performed. Young's moduli and Poisson's ratios of the microstructure are determined using homogenisation by asymptotic analysis. Four-point bending experiments are performed on the aluminium beams with the described microstructure. The same experiments are also performed numerically. Using the previously derived analytical expression for the strains in a plane orthotropic micropolar continuum, one characteristic length is determined. This length corresponds to the characteristic bending length in the isotropic continuum and is one of the four characteristic lengths of the planar orthotropic continuum. Experimental and numerical values agree well, despite the slight scatter of the experimental results. The methodology presented here can be used for further determination of bending lengths.

Key words: *orthotropic micropolar continuum, four-point bending experiments, characteristic bending length, homogenisation, numerical analysis*

Sažetak

U cilju dobivanja više mikropolarih inženjerskih parametara provedena je numerička i eksperimentalna analiza umjetno generirane ortotropne mikrostrukture. Youngovi moduli i Poissonovi koeficijenti mikrostrukture utvrđeni

[*] Sveučilište u Rijeci, Građevinski fakultet, Radmile Matejčić 3, 51000 Rijeka
E-mail: {damjan.jurkovic, gordan.jelenic, sara.grbcic, daragan.ribaric, laura.grbac, edita.papa, nina.ceh}@gradri.uniri.hr

su pomoću homogenizacije asimptotskom analizom. Eksperimenti čistog savijanja provedeni su na aluminijskim gredama s opisanom mikrostrukturom. Isti su eksperimenti provedeni numerički. Koristeći prije izvedene izraze za deformacije u ravninskom ortotropnom mikropolarnom kontinuumu određena je jedna karakteristična duljina. Ova duljina odgovara karakterističnoj duljini za savijanje u izotropnom kontinuumu i jedna je od četiri karakteristične duljine ravninskog ortotropnog kontinuuma. Eksperimentalne i numeričke vrijednosti dobro se poklapaju unatoč blagom rasipanju eksperimentalnih rezultata. Ovdje predstavljena metodologija može se koristiti za daljnje određivanje karakterističnih duljina.

Ključne riječi: *ortotropni mikropolarni kontinuum, eksperimenti čistog savijanja, karakteristična duljina za savijanje, homogenizacija, numerička analiza*

1. Introduction

Micropolar elasticity theory [1] has the capacity to describe materials with pronounced microstructure and sharp stress gradients more accurately. However, detection of the engineering parameters that describe micropolar continuum, of which there are six even in the simplest case of a linear elastic and centrosymmetric continuum, remains the leading barrier to its wider use.

It was shown in [2] that by solving the boundary value problem of cylindrical bending of a rectangular plate, one specific isotropic micropolar material parameter can be detected, from which we may identify the *characteristic length for bending*, directly responsible for the so-called *size effect*, whereby smaller specimens generally tend to be stiffer than larger ones. A procedure to detect the characteristic length for bending in two artificially created types of material with microstructure was presented in [3], where three-point bending experiments were conducted on a set of beam specimens of different sizes. An argument in favour of four-point bending was presented in [4] and verified against the results in [3]. However, both microstructures from [3] have some degree of orthotropy, which has motivated the current research, initiated in [5] and presented in [6], where a new simple orthotropic material model was designed. This model does not employ the full orthotropic micropolar continuum formulation as in [7] but a reduced one, with only one characteristic length for bending.

In this paper the material model from [6] combined with the methodology from [3] is used to detect the characteristic length of an artificially designed orthotropic micropolar continuum.

2. Material model

Material model that is used for detection of the characteristic length for bending is presented in [6]. We shall dub this model *reduced*, as orthotropy is assumed only in the constitutive tensor relating strains to stresses (and not in the one relating curvatures to couple stresses). Full orthotropic micropolar continuum, as presented in [7], would assume orthotropy in the latter as well. It is shown in [8] that this would then result in as many as four characteristic lengths for a plane-strain case. It should be noted that these papers do not differ between characteristic lengths for bending and torsion since it is questionable how such a distinction may be made for orthotropic continuum. Since the reduced model considered in this work was developed for the detection of characteristic length for bending from pure plate-bending experiments, it assumes boundary conditions in a state of plane strain. This leads to a reduction of material parameters needed to nine, with only one characteristic length for bending. Furthermore, the constitutive law for normal strains is assumed as [9]

$$\begin{Bmatrix} \epsilon_{xx} \\ \epsilon_{yy} \\ \epsilon_{zz} \end{Bmatrix} = \begin{bmatrix} \dfrac{1}{E_x} & -\dfrac{n_{yx}}{E_y} & -\dfrac{n_{zx}}{E_z} \\ -\dfrac{n_{xy}}{E_x} & \dfrac{1}{E_y} & -\dfrac{n_{zy}}{E_z} \\ -\dfrac{n_{xz}}{E_x} & -\dfrac{n_{yz}}{E_y} & \dfrac{1}{E_z} \end{bmatrix} \begin{Bmatrix} \sigma_{xx} \\ \sigma_{yy} \\ \sigma_{zz} \end{Bmatrix}, \tag{1}$$

where the constitutive tensor is known to be symmetric. This further reduces the number of independent parameters. Hence, to describe this continuum model, three Young's moduli, three Poisson's ratios and one characteristic bending length are needed. In [5,6], an analytical solution for strain at the edge of the beam subjected to pure bending has been derived as

$$\epsilon_{xx}(y = h/2) = \frac{(1 + \alpha_o)\psi_o}{1 + \alpha_o + \psi_o \delta} \frac{M}{\tilde{E}W}, \tag{2}$$

where α_o, ψ_o and $\tilde{E}$ are functions of the above-mentioned material parameters, defined in [9] as

$$\tilde{E} = \sqrt{\tilde{E}_x \tilde{E}_y}$$

$$\psi_o = \sqrt{\frac{\tilde{E}_y}{\tilde{E}_x}},$$

$$\alpha_o = \frac{\tilde{E}}{E_y}\left(n_{yx} + n_{yz}n_{zx}\right) = \frac{\tilde{E}}{E_x}\left(n_{xy} + n_{zy}n_{xz}\right), \tag{3}$$

$$\tilde{E}_x = \frac{E_x}{1 - n_{zx}n_{xz}},$$

$$\tilde{E}_y = \frac{E_y}{1 - n_{yz}n_{zy}}.$$

The extra material parameter δ depends on the characteristic length for bending l_b and the height of the beam:

$$\delta = 24\left(\frac{l_b}{h}\right)^2 \tag{4}$$

2.1 Geometry of microstructure

Figure 1 shows microstructure presented in [3] which is analysed in this paper. It consists of aluminium matrix with circular holes drilled so as to form a hexagonal pattern. The hole radius is $r = 3.5$ mm, the length of a unit cell $P_1 = 9$ mm and the height of a unit cell is $P_2 = 12.7$ mm. Similar microstructure with a different length of unit cell and, consequently, lower length to height ratio was able to be analysed as an isotropic micropolar material in [4].
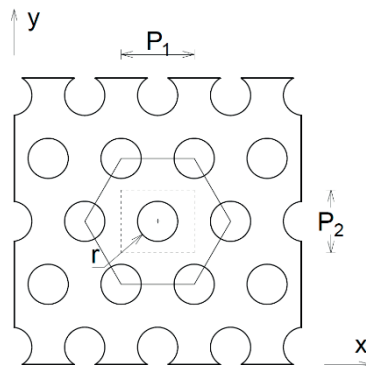
Figure 1. Geometry of the microstructure

All analysed samples have a width of 12.7 mm. Aluminium matrix is made from the EN-AW-6060-t66 alloy. From the tests performed on control (undrilled) specimens, Young's modulus of 72.399 GPa and Poisson's ratio of 0.3 have been obtained.

3. Representative-volume element (RVE) homogenisation

As this analysis considers the microstructure modelled as an orthotropic micropolar continuum, homogenisation of its engineering parameters needs to be carried out. With this in mind, a set of virtual experiments have been conducted. For this task, a representative-volume element (RVE) has been chosen as for a case of a square array of matrix inclusions [10], owing to the specific beam geometry with continuous longitudinal edges. An asymptotic analysis with RVEs of multiple sizes has been conducted and analysed for accuracy. The smallest RVE has been chosen as a unit cell shown in the centre of Figure 1. Other RVEs have been generated by multiplying number of rows and columns by a factor of two, i.e., 1x1, 2x2, 4x4, 8x8, 16x16 and 32x32, and named accordingly.

Virtual experiments have been performed using finite element method in FEAP [11]. The problem has been modelled as a plane stress problem in order to obtain all the material parameters from a unique experimental setup. The basic unit cell has been modelled using 116 nodes and 160 constant strain triangle (T3) elements. The meshes for other RVEs have been constructed by multiplication of unit cell mesh.

All RVEs have been axially loaded in a way that a continuous displacement is applied to one boundary of the specimen while the displacements in the same directions on the opposite boundary are restrained. In addition, two chosen nodes have the displacements in the orthogonal direction restrained as well to prevent rigid body motion. The same experiment is then repeated by rotating boundary conditions by 90°. Figure 2 shows one such experiment on unit cell (1x1 RVE).

The magnitude of the applied homogenous displacement $u_i = \varepsilon_i * l$ is chosen to provide the global homogenised normal strain $\varepsilon_i = 10^{-3}$. A resulting shortening in the orthogonal direction $u_{j,eq}$ is then obtained from the equivalent area bounded by the displacement curve of the unloaded edge $u_j(i)$. This value is used to calculate the homogenised strain in the orthogonal direction ε_j. The same procedure for attaining equivalent displacements is used to obtain equivalent reactions in the direction of loading $R_{i,ref}$ at the restrained nodes, used to calculate a homogenised stress σ_i in the direction of loading. Equivalently, the homogenised normal

strain ε_z is calculated from the volume equivalent to that bounded by the Gauss-point strains per element area.
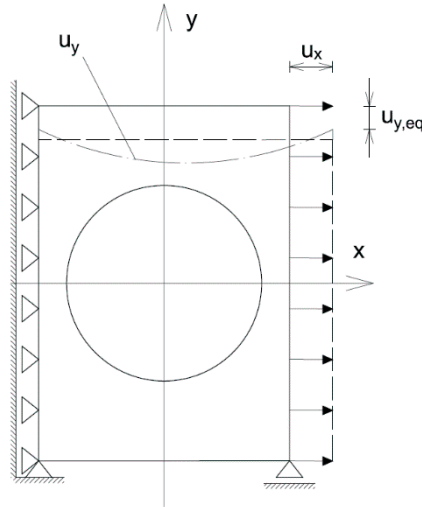
Figure 2. Axial tension virtual experiment on the unit cell (1x1 RVE)

From the computed values of stresses and strains the engineering parameters E_x, E_y, n_{xy}, n_{yx}, n_{xz} and n_{yz} follow as

$$E_i = \frac{\sigma_i}{\varepsilon_i} \tag{5}$$

$$n_{ij} = -\frac{\varepsilon_j}{\varepsilon_i}. \tag{6}$$

E_x, E_y, n_{xy} and n_{yx} are also calculated from averaged values of displacements and reactions along the edges. These values are compared to the values obtained before. It can be seen in Figure 3 that the difference between the values obtained using the two procedures converges towards zero as RVEs become larger. This convergence is slower for parameters E_y and n_{yx}, which use the displacements and reactions from the nodes on the edges with discontinuities. The same convergence does not happen with parameters n_{xz} and n_{yz} which remain in deviation of around 31.5% and 37% respectively. Note that here we do not compare the values obtained from average displacements but those obtained from average strains.

Young's modulus E_z is obtained analytically by comparing the areas of RVEs with holes with an equivalent rectangular area and is obtained as equal to 48.022 GPa for all specimens. For all the other engineering

parameters a pattern of convergence was noticed. Because of that, an asymptotic analysis was conducted. Based on the pattern of convergence, an inverse tangent function was chosen as a fitting function. Because of its different behaviour compared to other representative volumes, 1x1 RVE has not been included in the fitting procedure. Figure 4 shows fitting the E_x and n_{yz} values in this way. The fitting function is monotonically decreasing for parameters E_x, E_y and n_{yx} (only the first value shown), and monotonically increasing for n_{xy}, n_{xz}, and n_{yz} (only the last value shown). The 1x1 RVE results do not follow the monotonous converging trend for Young's moduli, but for Poisson's ratios it perfectly coincides with the fitting function, with largest error being in n_{yz} shown in Figure 4.
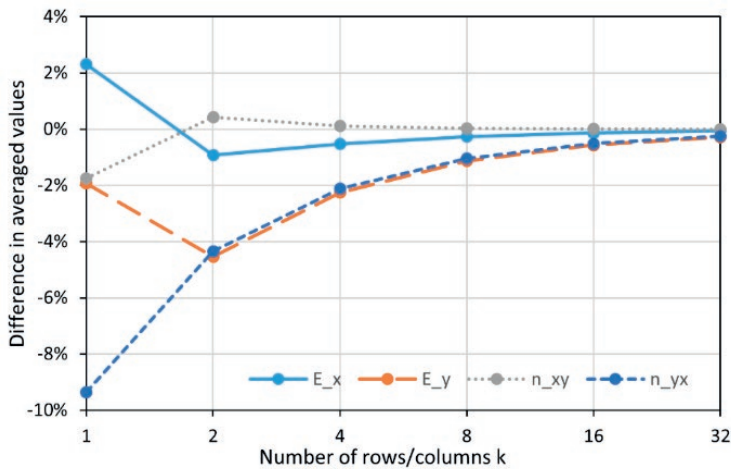
Figure 3. Convergence of material parameters obtained with different averaging

Now all that is left are two Poisson's ratios n_{zx} and n_{zy} which can be computed from (1). All computed parameters are displayed in Table 1.

Table 1. *Computed engineering parameters of the analysed microstructure*

$E_x[GPa]$	$E_y[GPa]$	$E_z[GPa]$	n_{xy}	n_{xz}	n_{yx}	n_{yz}	n_{zx}	n_{zy}
37.787	28.623	48.022	0.243	0.157	0.184	0.119	0.199	0.199

The symmetry of constitutive tensor from equation (1) can be used as a control term when substituting all precalculated values. This results in an error in symmetry of 0.26%, which is assumed to be a result of decimal rounding of the individual RVEs parameters substituted into the fitting

function. In [5], the homogenisation procedure was performed with homogenous boundary conditions without asymptotic analysis (just on a unit cell), which yielded an error of 46.22%, exposing the need for the present method. It should be noted that if the periodic boundary conditions had been applied to the RVE instead of the homogenous conditions, engineering parameters could have been determined from the 1x1 RVE. This is because periodic boundary conditions cancel the Saint-Venant principle [12]. Nevertheless, the analysis presented here is sufficient for this research.
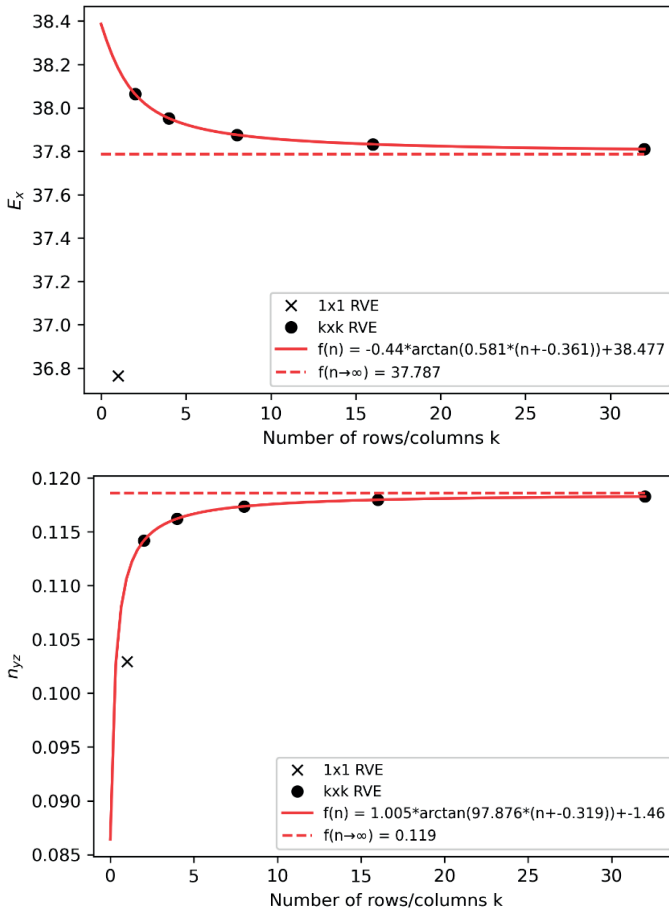
Figure 4. Asymptotic analysis of parameters E_x and n_{yz}

4. Four-point bending experiments on beam specimens

In an effort to detect the characteristic length for bending of our model, four-point bending experiments on the beams with described microstructure were conducted. The experiment performed here is equivalent to the one in [4]. Four-point bending load was applied as shown in Figure 5. The geometry from Figure 5 is given in Table 2. Depending on a number of rows of holes, four different beam types are analysed, named B1, B2, B3 and B4. Three specimens for each beam type are tested.
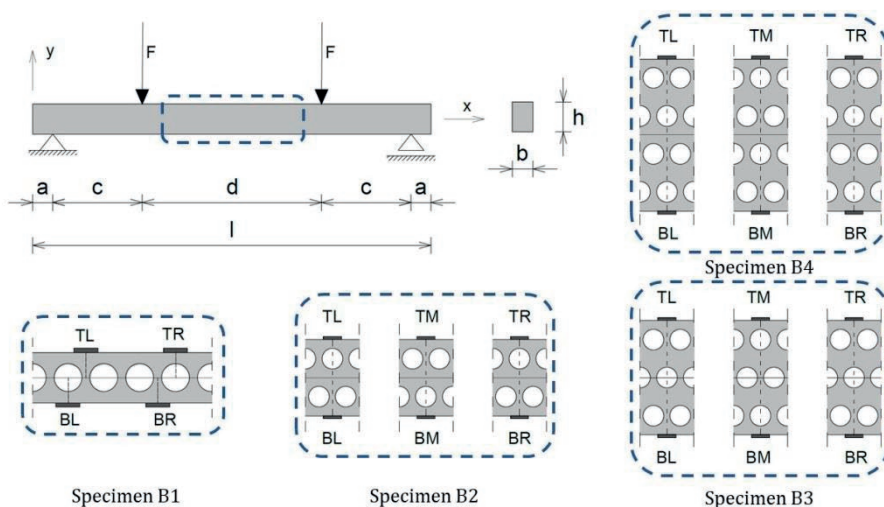
Figure 5. Representation of the four-point load experiments with disposition of strain gauges

Table 2. *Values from the experiment representation in Figure 5*

Sample	*l* [mm]	*h* [mm]	*b* [mm]	*d* [mm]	*a* [mm]	*c* [mm]	2*F* [kN]
B1	150	12.7	12.7	54	12	36	1.5
B2	280	25.4	12.7	128	10	66	2.5
B3	400	38.1	12.7	248	10	66	2.5
B4	530	50.8	12.7	297	13	103.5	5.0

Due to the specimen size, different specimens have been tested using different universal testing machines (UTMs) and load cells. Beam B1 is

tested using the load cell with capacity of 5 kN, beams B2 and B3 are tested using the load cell with capacity of 300 kN, and B4 using the load cell with capacity of 50 kN. Difference between load cell capacity and applied loads could be a factor in accuracy of the results. The beams are loaded with a loading speed of 10 N/s. The strains are recorded directly using HBM 6/120 LY43 strain gauges placed in the three cross sections, on top and bottom of the specimens (Figure 5). An exception is beam B1 which is too small to fit three strain gauges, so only two strain gauges have been placed on each boundary. The strain gauges are placed either closest to the drilled hole or halfway between two holes. This results in samples B2 and B4 having three strain gauges in the first position and another three in the second, B1 having two strain gauges in each position and B3 having two strain gauges in the first position and four in the second. It turns out that the strains at points closest to the drilled holes are smaller than those in between them. This is a result of the microstructure with a stress distribution mechanism which consists of compressive and tensile arches. GOM Aramis 12M optical system has been used for contactless measurement of kinematic field on the faces of specimens and displacement of the discrete point on the loading element of the UTM. The system uses 12 MP cameras with 4096 x 3000 resolution and pixel size of 3,45 μm. Optical measurements were caried out to measure the strains at the points where strain gauges have been placed via digital image corelation (DIC) method.

4.1 Virtual four-point bending experiments

The above-described experiments have been also simulated as virtual experiments. The meshes have been prepared as in Chapter 3, but this time twice as dense. Hence, e.g., the B1 mesh is made of 8,645 nodes and 15,104 elements, while the B4 mesh is made of 125,831 nodes and 226,560 elements. The need for such dense meshes comes from large stress gradient in the microstructure combined with poor behaviour of constant strain triangle (T3) elements in bending problems. However, with the aim of keeping the numerical model as simple as possible, such a model is sufficient at this stage of the research.

4.2 Postprocessing of the results

All force-displacement curves begin with nonlinear action that stabilizes over time. This is due to the so-called *take up of play*, during which the experimental setup assumes a stable position. In addition, it has been noticed that B2 beams have some nonlinear action at higher load values, and upon visual inspection it has been noticed that two specimens have some residual deformation. These effects were excluded from the

analysis as only the linear part of force-displacement curve is of interest. This was performed by calculating the slope in a linear part of a force-displacement curve smoothed out by a moving average convolution using ten data-points.

DIC measurement does not allow measuring displacements (and thus also strains) at the edge of a specimen. Because of the stress distribution mechanism of the microstructure mentioned earlier, it has been decided not to interpolate the edge values in this paper. The recorded values for the displacement at the loading points were processed in the same way as the DIC data.

Table 3 compares the measured values to the numerical ones. The measured values are taken as averages over three specimens. Large difference between the strain gauge and numerical strain data can be seen for the strain gauge values of B2 beam. It is assumed that a combination of plastic deformation and high noise from an inappropriate load cell has led to this result. Worsening of the UTM displacement result as the beams get smaller can be noted. Also, DIC measurement of the displacement at the point of force application yields results that are more in agreement with the numerical model.

Table 3. Deviation of the measured values from the numerical ones

Sample	B1	B2	B3	B4
Strain gauges [%]	2.8	28.5	2.2	5.9
UTM [%]	71.9	34.2	40.9	9.9
DIC [%]	16.8	26.6	32.9	0.3

5. Identification of the characteristic length for bending

It is possible to group all the engineering parameters within equation (2) into just one, homogenised Young's modulus, as

$$E_x^* = \frac{(1 + \alpha_o)\psi_o}{(1 + \alpha_o + \psi_o\delta)\tilde{E}} \tag{7}$$

When we substitute it back into (2), a well-known classical beam theory form is obtained as the result. When the bending moment $M = Fc$, the moment of resistance W and the average strain (considering the values nearest the holes and midway between them) ϵ_{xx} are substituted in (2), E_x^* is obtained. These values are shown in Table 4. Here index e next to a

beam type denotes an experimental result, while n denotes a numerical result. Dependence of E_x^* on $1/h^2$ is shown in Figure 6. It can be seen that the experimental data for B2, B3 and B4 samples manifest a *size effect* that is opposite to the one that occurs in the numerical results. Both experimental and numerical sets of data are interpolated using linear regression with the coefficient of determination (goodness-of-fit) and the linear equation parameters shown in Figure 6.

Table 4. Calculated values of homogenised Young's moduli

Sample	M [Nmm]	W [mm³]	ϵ_{xx} [/]	E_x^* [Pa]	$1/h^2$ [1/mm²]
B1$_e$	2,700	3,41.40	0.001198	64,630.882	0.00620
B1$_n$			0.001189	66,509.149	
B2$_e$	82,500	1,365.59	0.001331	43,963.946	0.00155
B2$_n$			0.001778	33,977.196	
B3$_e$	82,500	3,072.57	0.000646	40,092.177	0.00069
B3$_n$			0.000679	39,544.168	
B4$_e$	207,000	5,462.35	0.000943	38,733.437	0.00039
B4$_n$			0.000890	42,570.020	
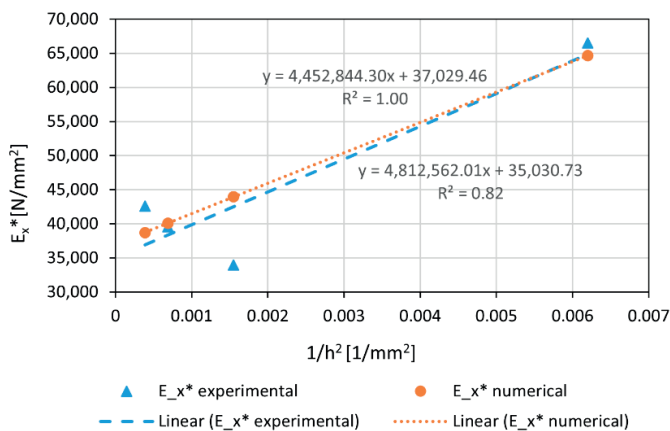
Figure 6. Homogenised Young's moduli for strain data

The material parameters that are contained within E_x^* can be separated into those that are dependent on $1/h^2$, and those that are not, and then equated to the linear equation representing the chosen regression pattern:

$$\frac{1}{\psi_o}\tilde{E} + \frac{24\psi_o}{(1+\alpha_o)\psi_o}\tilde{E}\left(\frac{l_b}{h}\right)^2 = \frac{A}{h^2} + B. \tag{8}$$

Equating the factors on both sides of the above equation dependent on $1/h^2$ provides the characteristic length for bending as

$$l_b = \sqrt{\frac{A(1+\alpha_o)}{24\tilde{E}}}, \tag{9}$$

while equating the constant terms give us a control equation

$$\frac{\tilde{E}}{\psi_o} = B, \tag{10}$$

which compares the engineering parameters derived via asymptotic analysis with the one derived from the pure-bending test. By substituting the known and computed material parameters into (9) and (10), the characteristic length for bending and a measure of its accuracy is obtained. For the existing experimental data, the characteristic length for bending is in the range between 2.705 and 2.731 mm depending on maximum and minimum values of the three specimens for each beam with the average value being 2.718 mm. The error in (10) is in the range between 8.20% and 12.03% depending on the three specimens results with the average value of 10.18%. The numerical analysis has provided the characteristic length for bending of 2.614 mm with an error of 5.06%. This error may have occurred because left hand side of the equation (10) was calculated using engineering parameters for infinitely large specimen which were acquired via asymptotic analysis in Chapter 3. It can be seen that these values are similar to those detected in [3], where isotropic formulation was used; $l_b = 2.28$ mm in the numerical analysis, and $l_b = 2.50$ mm for experimental values. The results obtained here are somewhat larger but the difference between the experimental and the numerical values is smaller. It should be noted that [3] uses a different definition of l_b which is denoted as l_b^* and which is connected to the one used here via $l_b = \frac{l_b^*}{\sqrt{24(1-n)}}$.

6. Alternative procedure for identification of the characteristic length for bending

Unfortunately, large difference between the strain-gauge data and the numerical data for specimen B2 has carried over to the accuracy of the characteristic length for bending. To resolve this problem, the approach used in [3] has been employed. The analytic expression for deflection at the loading point of a beam subjected to four-point bending is

$$w = \frac{Fc(3dc + 2c^2)}{6E_x^* I_z}. \tag{11}$$

This result has the same use as (2) after substituting E_x^*. Now it is again possible to calculate values of E_x^* by substituting all the known results and deflection w. These new values of E_x^* against $1/h^2$ are shown in Figure 7 for the UTM and the DIC displacement data. It can be seen that the DIC data are much more similar to the numerical results than the UTM data but none of them agree with the results obtained by the strain gauges.
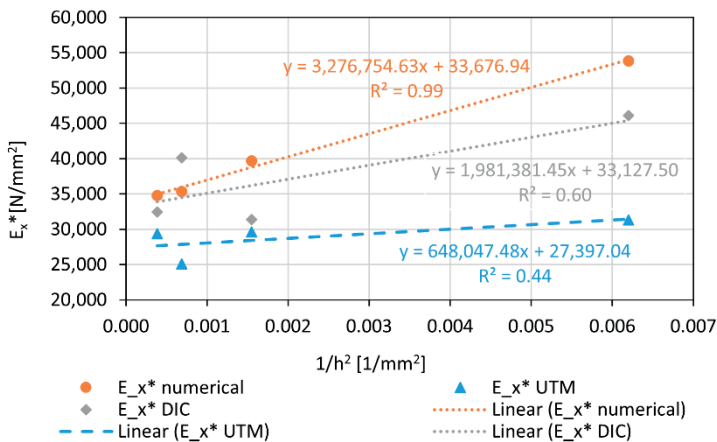
Figure 7. Homogenised Young's moduli for UTM and DIC displacement data

This can also be seen from coefficients of determination that is equal to 0.82 for strain gauges, 0.60 for DIC displacements and 0.44 for UTM displacement.

Upon further inspection of DIC data for the B1 beam sample it was noticed that displacement of the right-hand support had been included in the record. Although small, this displacement indicates certain compliance in the experimental setup. To account for this, that displacement has been subtracted from the total recorded displacement of the loading points.

Table 5 shows average values of differently obtained slopes of the force-displacement diagrams for beam B1, while their graphical representation is shown in Figure 8. It can be seen that the corrected DIC values are almost equal to the numerical results, with 97.85% equivalence, compared to 86.05% equivalence of the uncorrected DIC values. We can conclude that it is possible to filter out the effects of machine compliance in four-point bending test by measuring displacement in all four points via DIC.

Table 5. Slopes of force-displacement diagrams for sample B1

Method of measurement	UTM	DIC	Corrected DIC	Numerical
Slope [N/mm]	2,654.67	3,974.22	4,519.15	4,618.28
Slope / num slope [%]	57.48	86.05	97.85	100.00
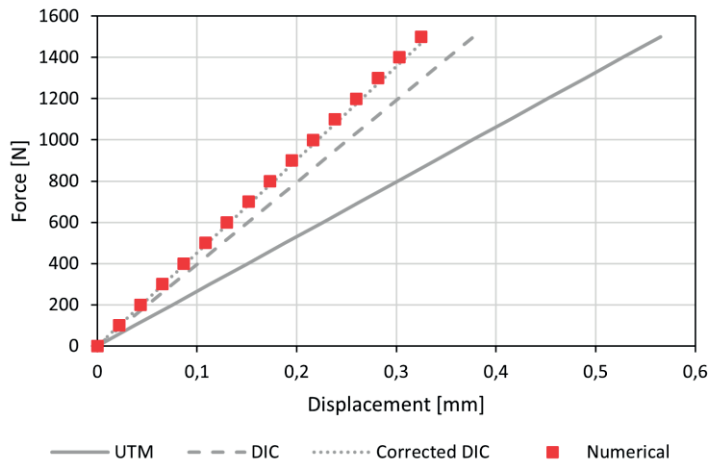
Figure 8. Comparison of different force-displacement diagrams for beam B1

7. Conclusion

The methodology presented in this paper utilises material model developed in [6] for detection of micropolar engineering parameters. It is shown that the mentioned reduced orthotropic micropolar continuum model provides a result of the characteristic length for bending for the analysed microstructure comparable to that in [3]. This confirms that the

presented methodology has a potential to be used for determination of the characteristic lengths in a full orthotropic micropolar continuum. Furthermore, the discrepancy between the experimentally and numerically captured size effects indicates the need for the usage of such a continuum. Anomalies that have occurred in the measurement of strains were attempted to be avoided using alternative techniques, by measuring the displacement. This did not result in a smaller error, which is probably due to the use of different load cells for different beams. Nevertheless, this analysis has shown that the optical measurement of the loading points in the four-point bending test via DIC can minimise the effects of the UTM compliance.

References

[1] Nowacki, W. (1972) Theory of Micropolar Elasticity. Vienna. Springer-Verlag.

[2] Gauthier, R.D., Jahsman, W.E. (1975) A Quest for Micropolar Elastic Constants. Journal of Applied Mechanics, 42(2), 369-374.

[3] Beveridge, A.J., Wheel, M.A., Nash, D.H. (2013) The Micropolar Elastic Behaviour of Model Macroscopically Heterogeneous Materials. International Journal of Solids and Structures, 50, 246-255.

[4] Papa Dukić, E., Grbac, L. Jelenić, G. (2024) Characteristic Bending Length In Micropolar Materials With Periodic Internal Structure. Journal of Mechanics of Materials and Structures, 19(3), 515-530.

[5] Jurković, D. (2022) Čisto savijanje u ortotropnoj mikropolarnoj elastičnosti. Master's thesis. University of Rijeka, Faculty of Civil Engineering.

[6] Jurković, D., Jelenić, G. Grbčić Erdelj, S. (2024) Analytical Solution for the Problem of Pure Bending of Orthotropic Micropolar Plate. Zbornik radova (Građevinski Fakultet Sveučilišta U Rijeci), 27(1)

[7] Alemi, B., Shodja, H.M. (2021) Effective Moduli and Characteristic Lengths of Micropolar Media with Dense Periodic Distribution of Ellipsoidal Nano-/Micro-Inhomogeneities. European Journal of Mechanics /A Solids, 85.

[8] Bouyge, F., Jasiuk, I. Boccara, S., Ostoja-Starzewski, M. (2002) A Micromechanically Based Couple-Stress Model of an Elastic Orthotropic Two-Phase Composite. European Journal of Mechanics /A Solids, 21, 465-481.

[9]   Jelenić G. (2021) On Pure Bending in Non-Linear Elasticity: A circular closed-form 2d solution for semi-linear orthotropic material. European Journal of Mechanics / A Solids, 90.

[10] Keane, A., Mccarthy, C., O'Dowd, Noel. (2008). The Effect of Matrix Non-linearity on the Properties of Unidirectional Composite Materials for Multi-Scale Analysis. Civil-Comp Proceedings, 88.

[11] Taylor, R.L., Govindjee, S. (2020) FEAP – A Finite Element Analysis Program. User manual. University of California at Berkeley. Berkeley.

[12] Hollister, S.J., Kikuchi, N. (1992) A Comparison of Homogenization and Standard Mechanics Analyses for Periodic Porous Composites. Computational Mechanics, 10, 73-95.